

## A SEARCH FOR MUON-ELECTRON AND MUON-POSITRON CONVERSION IN SULFUR

A. BADERTSCHER\*, K. BORER, G. CZAPEK, A. FLÜCKIGER,  
H. HÄNNI, B. HAHN, E. HUGENTOBLER, A. MARKEES\*\*,  
T. MARTI, U. MOSER, E. RAMSEYER, J. SCHACHER,  
H. SCHEIDIGER, P. SCHLATTER, G. VIERTEL\*\*\* and W. ZELLER

*Department of High Energy Physics, University of Berne, CH-3012 Berne, Switzerland*

Received 7 September 1981  
(Revised 2 November 1981)

**Abstract:** An experiment to search for the neutrinoless conversion of a muon into an electron or a positron in the processes  $\mu^- + {}^{32}\text{S} \rightarrow e^- + {}^{32}\text{S}$  and  $\mu^- + {}^{32}\text{S} \rightarrow e^+ + {}^{32}\text{Si}^*$  has been carried out at SIN. No evidence for the occurrence of these conversion processes has been found. The resulting new upper limits (under certain assumptions about coherence), relative to ordinary muon capture, are  $7 \times 10^{-11}$  (90% CL) for  $\mu^- \rightarrow e^-$  conversion and  $9 \times 10^{-10}$  (90% CL) for  $\mu^- \rightarrow e^+$  conversion. The measured momentum spectra of the electrons and positrons are compatible with the background spectra expected from bound muon decay and radiative muon capture.

E

NUCLEAR REACTIONS  ${}^{32}\text{S}(\mu^-, e^\pm), E=0$ ; measured  $e^-, e^+$  spectra; deduced upper limits for  $\mu^- + {}^{32}\text{S} \rightarrow e^- + {}^{32}\text{S}$  and  $\mu^- + {}^{32}\text{S} \rightarrow e^+ + {}^{32}\text{Si}^*$ .

### 1. Introduction

The search for the conversion of muons into electrons is an important experimental test of theories of the electroweak interaction. Many years ago, the apparently identical interaction behaviour of electrons and muons (muon-electron universality) had suggested the idea of the muon as an electromagnetically excited state of the electron. This speculation however soon proved to be in conflict with experimental results and theoretical ideas. The advent of intermediate vector bosons (IVB) in weak interaction theory led to the prediction<sup>1,2)</sup> of cutoff-dependent finite rates for  $\mu \rightarrow e\gamma$ ,  $\mu \rightarrow eee$  and  $\mu^- \rightarrow e^-$  conversion, which were thought to occur via a neutrino-plus-vector-boson intermediate state. The fact that none of these processes were observed could only be explained by postulating the existence of more than one type of neutrino, a hypothesis which later on was verified in neutrino experiments<sup>3)</sup>. The existence of different neutrino states led to the introduction of conserved leptonic quantum numbers. Assigning  $L_e = 1$  to  $\nu_e$  and  $e^-$ ,  $L_\mu = 1$  to

\* Present address: Los Alamos National Laboratory, Los Alamos, NM 87545, USA.

\*\* Institut für Experimentalphysik V, Universität Dortmund, D-4600 Dortmund, Germany.

\*\*\* CERN-ETHZ, CH-1211 Genève 23, Switzerland.

$\nu_\mu$  and  $\mu^-$ , and the opposite lepton numbers to the antiparticles, the following three lepton number conservation schemes have been proposed:

(i) The additive law, which requires both  $\sum L_e$  and  $\sum L_\mu$  to be separately conserved. This scheme can easily be generalized to more than two lepton generations.

(ii) The multiplicative law<sup>4)</sup>, which requires  $\sum(L_e + L_\mu)$  and the product of the muon parities  $(-1)^{L_\mu}$  to be conserved. This scheme can be extended to include the third generation of leptons<sup>5)</sup>. Experimental bounds on rates of processes allowed by the multiplicative law only are at the level of 5% of the normal weak decays<sup>6)</sup>.

(iii) The Konopinski-Mahmoud scheme<sup>7)</sup>, which requires  $\sum(L_e - L_\mu)$  to be conserved. A possible way to include the third lepton family is indicated in ref.<sup>8)</sup>.

Muon-electron conversion as well as  $\mu \rightarrow e\gamma$ ,  $\mu \rightarrow \text{eee}$  and  $K_L^0 \rightarrow \mu e$  are forbidden by all of the three schemes, in contrast to muon-positron conversion, which is not forbidden by the Konopinski-Mahmoud scheme. Up to now there has been no experimental evidence for the existence of muon number violating processes. The present upper limits (90% CL) for the processes mentioned before are:

$$R_{\mu \rightarrow e\gamma} = \Gamma(\mu \rightarrow e\gamma)/\Gamma(\mu \rightarrow \text{all}) < 1.9 \times 10^{-10} \quad [\text{ref. } 9)],$$

$$R_{\mu \rightarrow \text{eee}} = \Gamma(\mu \rightarrow \text{eee})/\Gamma(\mu \rightarrow \text{all}) < 1.9 \times 10^{-9} \quad [\text{ref. } 10)],$$

$$R_{K_L \rightarrow \mu e} = \Gamma(K_L \rightarrow \mu e)/\Gamma(K_L \rightarrow \text{all}) < 2 \times 10^{-9} \quad [\text{ref. } 11)],$$

$$R_{\mu^- \text{Cu} \rightarrow e^- \text{Cu}} = \Gamma(\mu^- \text{Cu} \rightarrow e^- \text{Cu})/\Gamma(\mu^- \text{Cu} \rightarrow \nu_\mu + \dots) < 1.6 \times 10^{-8} \quad [\text{ref. } 12)].$$

In addition, muon-electron universality has been tested to the  $10^{-5}$  level in electromagnetic interactions [muonic ( $g-2$ ) experiment<sup>13)</sup>] and to the percent level in weak interactions [branching ratio of  $\pi \rightarrow e\nu$  versus  $\pi \rightarrow \mu\nu$ , ref.<sup>14)</sup>]. However, the conservation of lepton numbers as well as muon-electron universality are not sacred principles in gauge theories of the electroweak interactions, in which both may be violated in a natural way<sup>15)</sup>, their observed approximative validity being the consequence of some suppression mechanism rather than of a conservation law.

In the standard  $SU(2) \times U(1)$  model of Salam and Weinberg<sup>16)</sup> with only one Higgs doublet, the lepton numbers are all automatically conserved, because the neutrinos are all massless. However, this minimal model can easily be generalized by admitting massive neutrinos. If not degenerate, these neutrinos will in general be mixed in analogy to the quarks, inducing thereby<sup>17)</sup> the violation of muon-number conservation, e.g. in  $\mu^- \rightarrow e^-$  conversion (fig. 1a).

The standard model can also be enlarged by introducing further Higgs doublets. The Higgs-lepton coupling may then mediate  $\mu^- \rightarrow e^-$  transitions<sup>18)</sup>.

The existence of additional Higgs bosons or of massive neutrinos may be associated with group structures beyond  $SU(2) \times U(1)$ , such as<sup>19)</sup>  $SU(2)_L \times SU(2)_R \times U(1)$  or the groups of grand unified theories<sup>20)</sup>.

Attempts have been made to understand the occurrence of similar generations of quarks and leptons as an indication of an underlying horizontal gauge symmetry.

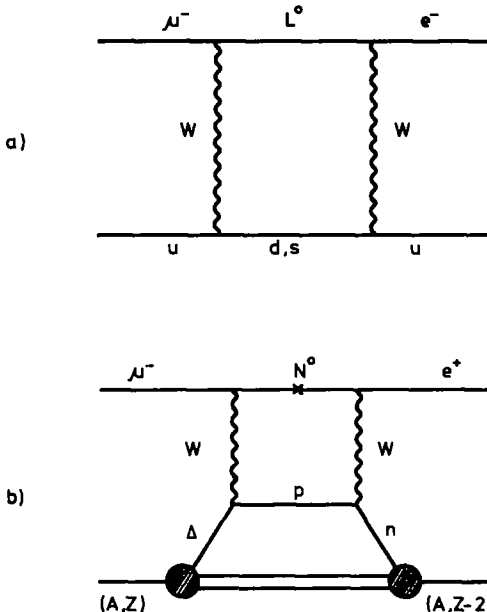


Fig. 1. Typical Feynman diagrams (a) for nuclear  $\mu^- \rightarrow e^-$  conversion in models with neutral heavy leptons  $L^0$  of Dirac or Majorana type, and (b) for nuclear  $\mu^- \rightarrow e^+$  conversion in models with neutral heavy Majorana leptons  $N^0$ .

The corresponding generation changing neutral gauge bosons can mediate  $\mu \rightarrow e$  transitions<sup>21)</sup>. Such bosons also occur in theories<sup>22,23)</sup> with a dynamical symmetry breaking mechanism (technicolor theories). In most of the proposed models, muon-electron conversion is expected<sup>24)</sup> to occur on a higher level than  $\mu \rightarrow e\gamma$  and  $\mu \rightarrow eee$ . From 1952, when the first muon-electron conversion experiment<sup>25)</sup> was realized, to 1972, when the last one was carried out<sup>12)</sup>, the upper limit for this process steadily<sup>26,27)</sup> dropped by more than six orders of magnitude to the value of  $1.6 \times 10^{-8}$  obtained for a copper target. The aim of the experiment described in this paper was to search for muon-electron conversion with a sensitivity of at least two orders of magnitude below this level.

In contrast to  $\mu^- \rightarrow e^-$  conversion, the observation of  $\mu^- \rightarrow e^+$  conversion would signal a breakdown not only of the separate electron- and muon-number conservation, but also of the total lepton-number conservation. A Majorana mass term<sup>28)</sup> for neutrinos, violating the conservation of the total lepton number by two units, may induce  $\mu^- \rightarrow e^+$  conversion in nuclei as a higher-order weak process involving either two nucleons<sup>29)</sup> or a virtual  $\Delta^{++}$  (fig. 1b) in the nucleus<sup>30)</sup>. The observation of  $\mu^- \rightarrow e^+$  conversion would imply a positive rate at some level for processes such as  $\mu \rightarrow e\gamma$ ,  $\mu \rightarrow eee$  and  $\mu^- \rightarrow e^-$  conversion, whilst the reverse is not true, since these latter processes may occur independently of whether the neutrinos in the

intermediate state are of Dirac or Majorana type.  $\mu^- \rightarrow e^+$  conversion may also be caused by additional charged Higgs fields in the standard model<sup>31)</sup>.

Upper limits for muon-positron conversion can be deduced<sup>32)</sup> from early experiments<sup>27)</sup> looking for muon-electron conversion, in which also positrons would have been detected. The first and thus far only experiment<sup>12)</sup>, explicitly searching for muon-positron conversion was carried out in 1972. It established the upper limit

$$R_{\mu^- \text{Cu} \rightarrow e^+ \text{Co}} = \Gamma(\mu^- \text{Cu} \rightarrow e^+ \text{Co}^*) / \Gamma(\mu^- \text{Cu} \rightarrow \nu_\mu + \dots) < 2.6 \times 10^{-8} \text{ (90% CL).}$$

This paper gives a full account of an experiment carried out at SIN, which simultaneously searched for  $\mu^- \rightarrow e^-$  and  $\mu^- \rightarrow e^+$  conversion. Sect. 2 is devoted to a detailed description of the experimental procedure. In sect. 3, background processes to  $\mu^- \rightarrow e^-$  and  $\mu^- \rightarrow e^+$  conversion are discussed. The Monte Carlo simulation of these background processes and of the hypothetical conversion process is explained in sect. 4. The results of the experiment<sup>33,34)</sup> are given in sect. 5 and discussed in the last section.

## 2. Experimental technique

### 2.1. METHOD

The realization of a new generation of experiments searching for  $\mu \rightarrow e$  transitions with considerably increased sensitivity was made possible by the construction of the meson factories LAMPF, SIN and TRIUMF. This experiment was carried out at SIN, making use of a high-intensity muon beam.

In muon-electron conversion, the atomic number  $Z$  remains unchanged, contrary to ordinary muon capture. If the nucleus is not excited by the conversion process, the electrons emitted in  $\mu^- \rightarrow e^-$  conversion are monoenergetic with an energy of 104.7 MeV for a sulfur target. A theoretical lower bound of 83% has been established<sup>2)</sup> for this coherent part of the process. Moreover, electron-sulfur scattering<sup>35)</sup> at the same momentum transfer proved to be almost totally elastic. Based on these data, we assume the coherent part to be 100%.

Contrary to  $\mu^- \rightarrow e^-$  conversion, there is an almost complete lack of information on the momentum spectrum of  $\mu^- \rightarrow e^+$  conversion positrons. The mean positron momentum is shifted away from the maximum (101.8 MeV for sulfur) due to the excitation of the nucleus involved. Since there are no theoretical predictions on this excitation, the only useful hint is given by the mean nuclear excitation energy in ordinary muon capture, which is<sup>36)</sup> around 15 MeV for sulfur. The mean excitation energy for muon-positron conversion, which involves a change in the nuclear charge by two units instead of one, is expected to be somewhat larger. We consider a mean excitation energy of  $\bar{E}^* = 20$  MeV to be a reasonable assumption.

The design of the setup (figs. 2, 3) was such as to take advantage of the clear experimental signature of the process searched for, i.e. an electron or a positron

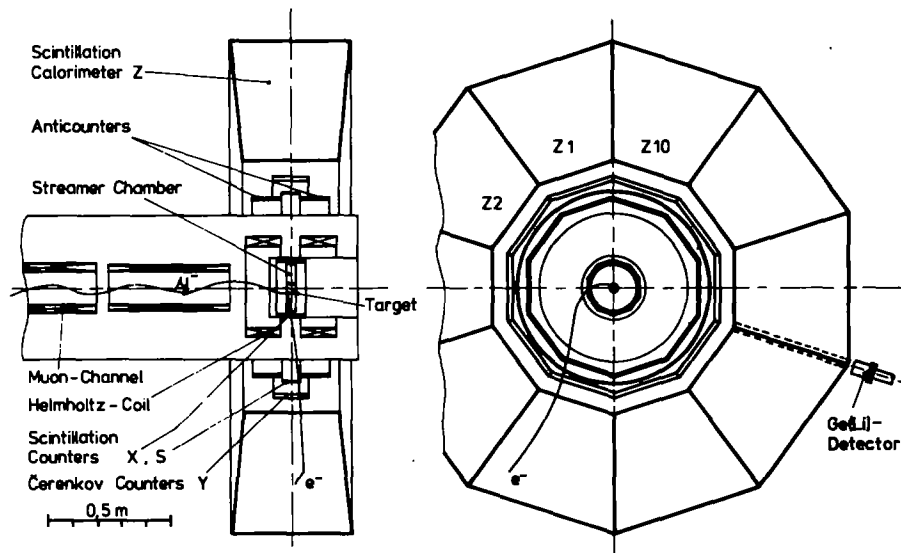


Fig. 2. Muon channel and ring detector (with streamer chamber, trigger counters and calorimeter). A track of an electron from the hypothetical reaction  $\mu^- + ^{32}\text{S} \rightarrow e^- + ^{32}\text{S}$  is shown in both views.

with an energy of about 100 MeV. The detection system, covering a relative solid angle of 12%, was built concentrically around a hollow-cylindrical sulfur target mounted inside a small cylindrical streamer chamber. With the high-intensity muon beam, stop rates of the order of  $10^6/\text{s}$  were achieved. The streamer chamber, which was used to measure the momenta of secondary particles, was placed inside a superconducting double coil and photographed by three cameras equipped with image intensifiers. Interesting events could then be evaluated off-line. Charged particles produced in the target with momenta less than about  $70\text{ MeV}/c$  were trapped by the strong magnetic field (3.5 T) and did not reach the trigger counters arranged concentrically around the streamer chamber. The trigger system consisted of several rings of scintillation counters, Čerenkov counters and scintillation calorimeters (fig. 2). To allow a first crude momentum selection, the counter rings were subdivided into 10 independent segments. The scintillation calorimeters were also used to discriminate against low-energetic background and to measure roughly the energy of selected events. The number of muon captures was determined by means of a Ge(Li) detector, using the 1.27 MeV  $\gamma$ -transition  $^{31}\text{P}^* \rightarrow ^{31}\text{P} + \gamma$  which follows the capture process  $\mu^- + ^{32}\text{S} \rightarrow \nu_\mu + ^{31}\text{P}^*$ . Cosmic-ray muons and electrons were strongly suppressed by proper anticounters. In addition, the whole apparatus was shielded against fast neutrons by iron and heavy concrete.

Absolutely essential to the success of the experiment was the pulsing of the primary proton beam. Without pulsing, a disastrous background would have come from radiative pion capture with a photon converting internally or externally into

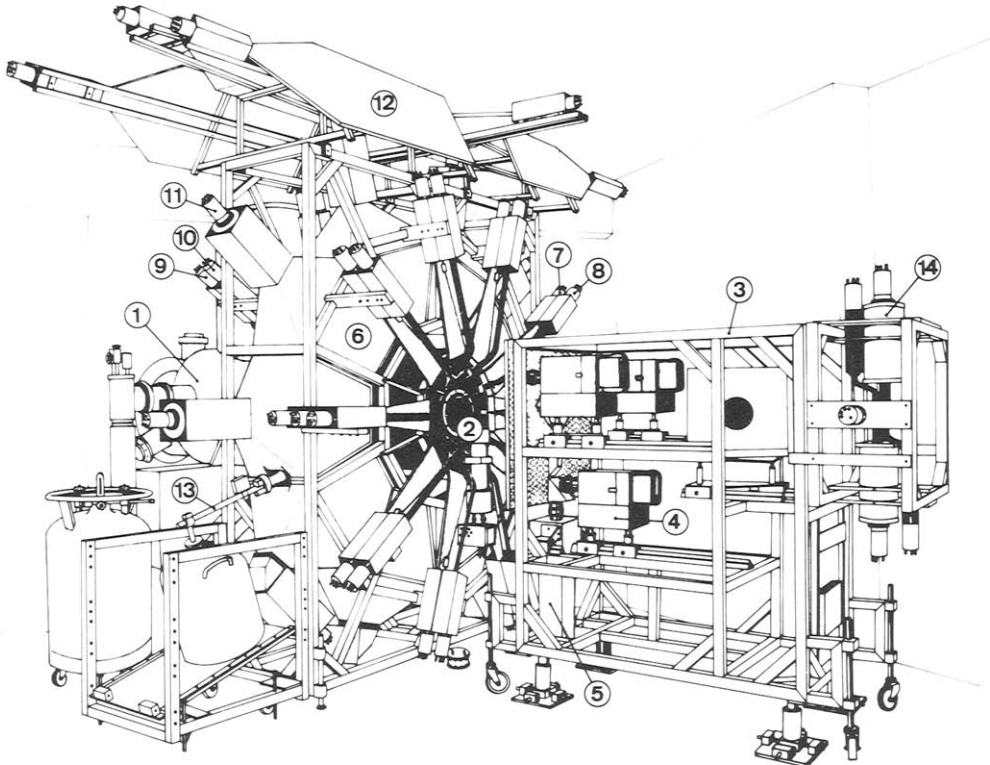


Fig. 3. View of the apparatus: (1) muon channel, (2) streamer chamber system, (3) optics rack, (4) image intensifier cameras, (5) image intensifier with TV camera (nocticon), (6) calorimeter block, (7) photomultiplier of anticounter, (8) photomultiplier of X-counter, (9) same as (7), (10) photomultiplier of Y-counter, (11) photomultiplier of calorimeter block, (12) roof of anticounters, (13) Ge(Li) detector and (14) telescope to measure the beam suppression.

an asymmetric electron-positron pair. To reach conversion branching ratios of the order of  $10^{-10}$ , the pion intensity had to be reduced by at least a factor of  $10^7$ . To this end, a special beam pulser was constructed by SIN<sup>37</sup>).

## 2.2. BEAM

The experiment was run at the secondary pion beam line  $\mu\text{E}4$  (fig. 4). This beam, starting under a  $90^\circ$  angle from a 12 cm thick Be production target, was transported through a quadrupole triplet to a bending magnet, where it was deflected by additional  $45^\circ$  to reach the carbon degrader, located at the upstream end of the superconducting muon channel<sup>38</sup>). In the muon channel, a large fraction of the pions decayed into muons. The beam optics was set for a negative beam and optimized to produce a maximum rate of stopped muons on the target inside the

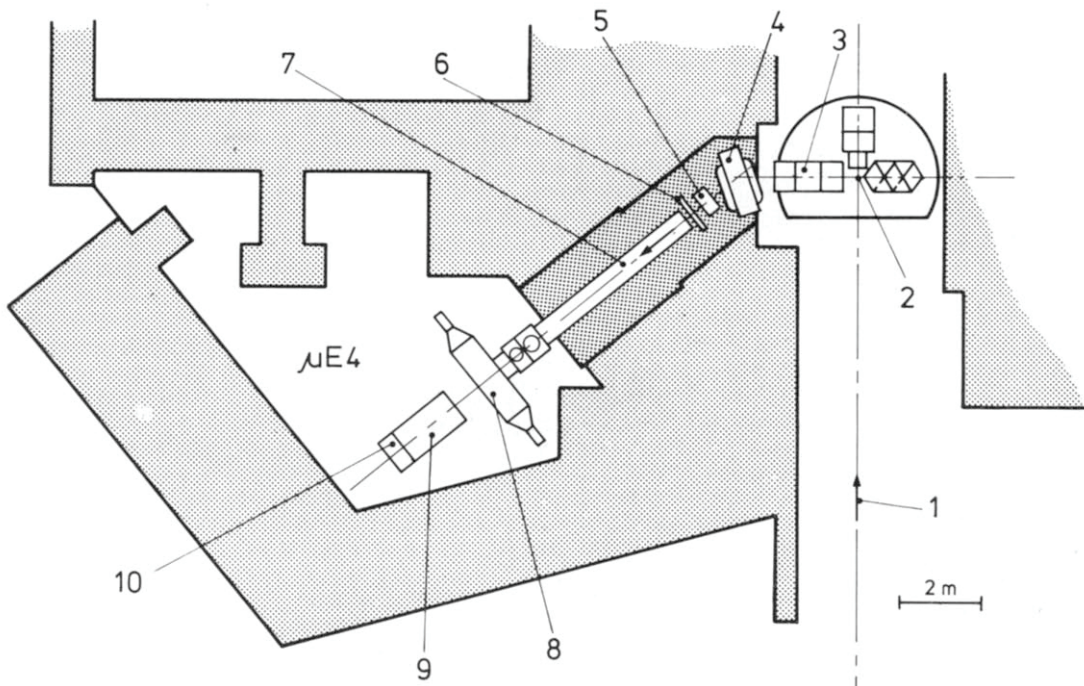


Fig. 4.  $\mu\text{E}4$  area at SIN. The figure shows (1) the incoming proton beam, (2) the production target, (3) the quadrupole triplet, (4) the bending magnet, (5) the beam stop, (6) the degrader, and (7) the superconducting muon channel. In the experimentation area, the ring detector with the double-coil magnet ANDROMEDA (8), the optics rack (9) and the telescope to measure the beam suppression (10) are shown.

double-coil magnet. Maximum stop rates ( $\sim 10^6/\text{s}$ ) were obtained for a beam momentum of  $120 \text{ MeV}/c$  ( $\pm 4\%$ ) and a  $6.5 \text{ g/cm}^2$  thick carbon degrader. To suppress the prompt background, the primary proton beam was pulsed with a frequency of  $400 \text{ kHz}$ , adapted to the disappearing rate of muons in sulfur. During the beam-on time ( $\sim 1 \mu\text{s}$ ), stopped muons were accumulated in the target. Their decay was then observed in a measuring gate in the beam-off period. A beam-suppression factor of the order of  $10^7$  was achieved by pulsing the ion source of the injector cyclotron and by deflecting the accelerated beam upstream of the production target by a specially designed <sup>34)</sup> electrostatic deflector. The suppression factor was measured on-line with a counter telescope (see subsect. 2.6). Due to the pulsing, the average intensity of the primary proton beam was limited to about  $40 \mu\text{A}$ .

### 2.3. DOUBLE COIL

A superconducting double-coil magnet <sup>38)</sup> (similar to a Helmholtz pair) called ANDROMEDA was used as a magnetic spectrometer. It was coupled magnetically,

cryogenically and mechanically to the 5 m long SIN muon channel (fig. 4) to guarantee an optimal transport of the muons to the target.

The principles of the experiment (trapping of low-momentum background, rough energy determination with calorimeters, precise momentum measurement with a streamer chamber) led to the following requirements for the double-coil:

- (i) inside the cryostat of the magnet, space had to be available for a small streamer chamber operated at room temperature;
- (ii) outside the cryostat, starting from a radius of about 30 cm and over an azimuth angle of 360°, there had to be room for the installation of trigger and calorimeter counters in the radial direction;
- (iii) magnetic field volume for experimentation: 15  $\ell$ ;
- (iv) maximum magnetic flux density: 4.5 T;
- (v) field inhomogeneity less than 2% in a cylindrical volume of 0.5  $\ell$ ;
- (vi) current instability less than 1%, during 8 h.

The muon channel and the double coil were cooled by forced supercritical cooling ( $\sim 40$  W) and by helium-bath cooling ( $\sim 5 \ell/\text{h}$  at 4.5 T), respectively. To avoid too much energy loss, the amount of material between the target and the trigger counters had to be kept at a strict minimum. On the average, a particle from the target had to pass through  $2 \text{ g/cm}^2$  of absorbing material (0.3 radiation lengths) before reaching the calorimeter counters. This absorbing material included the 3.5 mm thick cylindrical sulfur target, the streamer chamber wall (1 mm of plexiglas), the 6 mm thick epoxy hard-glass support ring used as a spacer between the double-coil halves, and 0.3 mm of stainless steel.

Most of the data were taken at a magnetic field of 3.5 T in the double coil and of 4.5 T in the SIN muon channel.

## 2.4. STREAMER CHAMBER

**2.4.1. Chamber body.** A cylindrical streamer chamber (20 cm diameter, 4 cm depth) was used to visualize the tracks and to measure the momenta of secondary electrons and positrons. It had two gaps (2 cm each), the central electrode being connected to high voltage. By operating the chamber in the avalanche mode, the streamers were kept small enough (1 mm in diameter, 2 mm in the field direction) to allow accurate momentum measurements. Together with the HV transmission line, the streamer chamber had to fit into the small pot inside the superconducting double-coil magnet. To keep the chamber mass as low as possible, the chamber body was made out of thin lucite rings, the chamber windows out of  $3 \mu\text{m}$  thick mylar foils, and the electrodes out of  $5.4 \text{ mg/cm}^2$  of stainless steel-net with 90% transparency.

**2.4.2. Target.** A hollow-cylindrical sulfur target (40 mm in diameter, 40 mm long, 3.5 mm thick) with a mass of 28 g was centered inside the sensitive volume of the streamer chamber.

The target material sulfur was chosen to optimize the muon capture rate in the measuring gate. As the muon capture rate  $\Gamma_{\text{capt}}$  increases strongly with  $Z$ , a large  $\Gamma_{\text{capt}}/\Gamma_{\text{decay}}$  ratio implied the use of a heavy nucleus. On the other hand, the lifetime of the bound muons had to be sufficiently long in order not to lose too many muons before the opening of the measuring gate. In addition, the target material had to be an excellent insulator. Under these conditions, sulfur was the optimal choice. Natural sulfur consists of 95%  $^{32}\text{S}$ , which is an isoscalar isotope.

The choice of a hollow-cylindrical target shape was the result both of stop-rate measurements and of Monte Carlo calculations of the beam transport down the muon channel and the energy loss of secondary particles in the target.

**2.4.3. High-voltage pulse system.** The nanosecond pulses necessary to operate the streamer chamber were generated by a seven-stage Marx generator [similar to the one described by Gygi and Schneider<sup>39</sup>], which was connected to the pulse-forming charge line through an inductor (fig. 5). Within 25 ns after firing the Marx generator, the potential at the spark gap raised to a value of 100 kV. The two spark gap electrodes were separated by 1 mm and kept in a SF<sub>6</sub> atmosphere at 6 bar. The charge line, a coaxial 20  $\Omega$  line, was made 23 cm long to get a pulse length of 3 ns in the silicon-rubber dielectric. High-voltage pulses measured at the charge line and at the 20  $\Omega$  transmission line are shown in fig. 5.

The trigger generator, which worked with two UHF-planar triodes in cascade connection<sup>40</sup>), had a delay time of 16 ns. The total delay time of the system was about 100 ns.

**2.4.4. Gas system.** The streamer chamber was operated with a gas mixture of 70% Ne and 30% He at atmospheric pressure. The resulting memory time of  $\sim 200 \mu\text{s}$  had to be reduced because of the high beam intensity ( $\sim 10^7$  particles/s), which otherwise would have caused the appearance of many old tracks on the streamer chamber pictures. By adding<sup>41</sup>) a small fraction ( $\sim 0.25$  ppm) of SF<sub>6</sub> it could be lowered to  $\sim 800$  ns, which was small enough to get reasonably clean and well measurable photographs (fig. 6), with a streamer density of 3–4/cm. The memory time was measured with a special ionization chamber<sup>41</sup>) containing a 1 mCi source of  $\alpha$ -particles ( $^{241}\text{Am}$ ). Electrons produced by ionization were partly absorbed by the SF<sub>6</sub> molecules, so that the current in the ionization chamber was a direct measure of the memory time. Deviations from a reference value caused a valve to be opened and additional SF<sub>6</sub> to be added to the chamber gas.

**2.4.5. Photographic registration of tracks.** Because of their low light yield, the streamers could not be photographed directly. They were intensified by a system of three consecutive image tubes with electrostatic focusing (Mullard XX 1050). To avoid blackening of the film by tube noise, the third stage was pulsed electrically. With this setup, the streamer light energy was intensified by approximately a factor of 1000. The image tubes were protected from the magnetic stray field ( $\sim 0.02$  T) by a  $\mu$ -metal shield and by an outer double-walled soft-iron housing (10 mm wall thickness). However, the residual stray field still caused a slight rotation of the

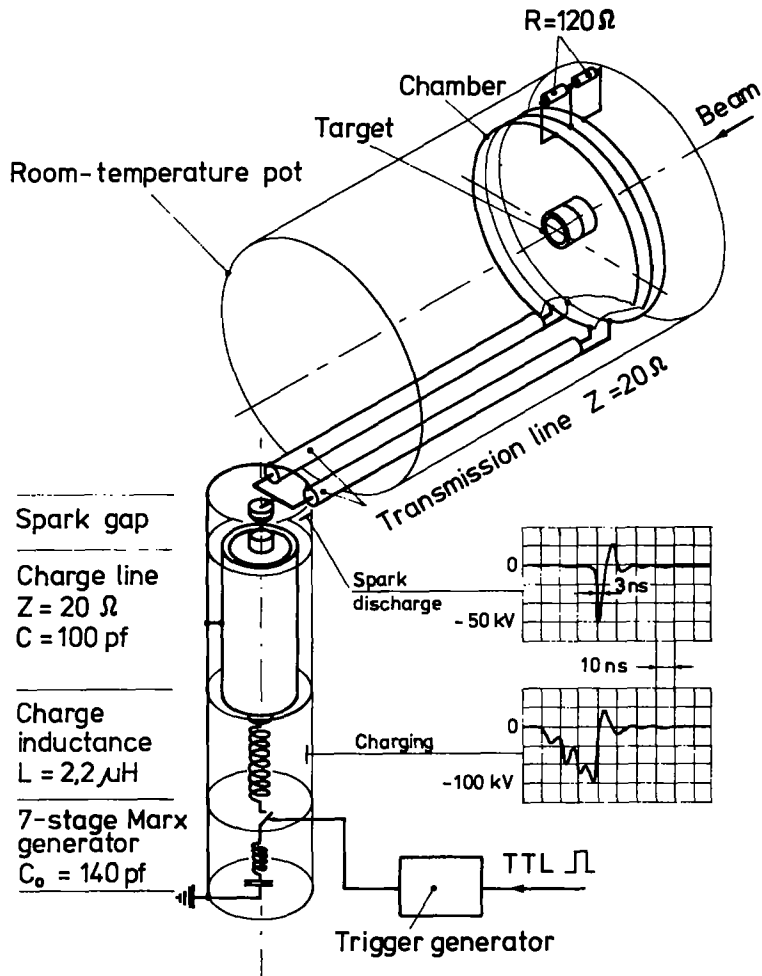


Fig. 5. Equivalent circuit of the Marx generator and the pulse-forming network. Typical high-voltage pulses at the charge line and at the transmission line are shown.

pictures around the central axis of the image tubes. The image tubes themselves led to a pin-cushion distortion, which had to be corrected off-line. To this end, an orthogonal, rectangular reference grid was photographed periodically.

The streamer chamber was photographed in stereo from a distance of 1.5 m by three cameras equipped with 2.8/120 Biometar objectives (Zeiss Jena), resulting in a scale factor of 0.08 and a maximal depth of focus of 42 mm (at an assumed aberration disk diameter of 45  $\mu\text{m}$ ). Two streamers separated by more than 0.4 mm in the streamer chamber could be resolved as two different track points on the film (Kodak RAR 2496).

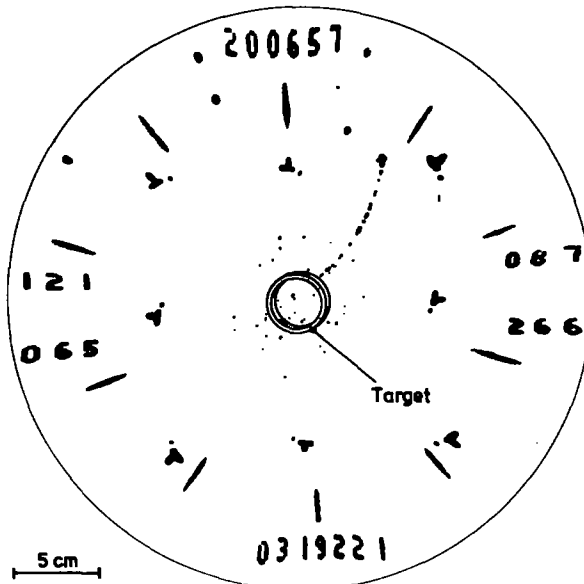


Fig. 6. Typical streamer chamber picture at a beam intensity of  $26.6 \mu\text{A}$  proton current. The track is due to an electron from bound muon decay in sulfur.

The operating condition of the streamer chamber was continuously monitored by a TV system via a mirror with 50% reflectance mounted in front of one of the three cameras (fig. 3). The TV system consisted of a microchannel image tube (Mullard XX 1360), a pulsed normal image tube and a TV nocticon (Thomson CSF TH 9659), which was part of a normal TV camera (Grundig Fernauge FA 32). An image-storing device (Thomson CSF TH 7001) permitted examination of single standing pictures. The direct visual control of the streamer chamber turned out to be of crucial importance.

## 2.5. COUNTERS AND CALORIMETER

To generate the event trigger, a system consisting of four rings of trigger counters with several additional anticounters against cosmic rays was arranged concentrically around the target (figs. 2, 3). The trigger counter rings were placed either inside (3 mm thick scintillation counters X) or outside the double-coil magnet (3 mm thick scintillation counters S, 2 cm thick lucite Čerenkov counters Y, 50 cm thick scintillation calorimeter blocks Z). Each counter ring, except the S-ring, was subdivided into 10 segments. The photomultipliers were protected from the stray field of the magnet by long light pipes and by iron shieldings.

The calorimeter ring Z, consisting of scintillator blocks (fig. 7) large enough to absorb electrons up to an energy of 100 MeV, had to reject triggers from low

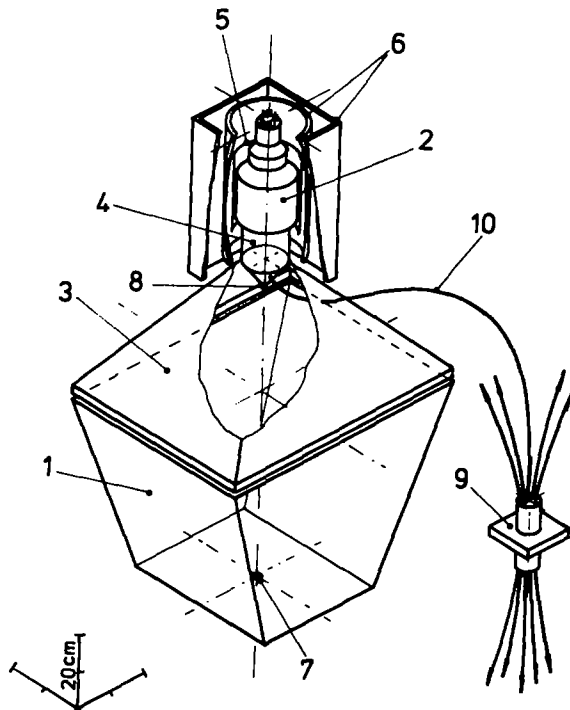


Fig. 7. Calorimeter block: a scintillator block (1) (Ne 102A), which was covered on five sides with reflecting aluminium foil, was connected to a photomultiplier (2) (Philips 58DVP) through an internally white-painted air light pipe (3) and a piece of lucite (4) (used to increase the light collection efficiency). The photomultiplier was protected from the stray field of the magnet by  $\mu$ -metal (5) and soft-iron shielding (6). A separate 30 kHz LED pulser (7) was installed in every block to stabilize the anode current. To monitor the gain, each block was equipped with an Am pulser (8) and connected to a central LED pulser (9) by Crofon light fibres (10).

energetic background. To detect events occurring in more than one block, the photomultiplier (Philips 58DVP) anode signals of each of three adjacent calorimeter counters were added up and put into discriminators. An energy deposition of at least 55 MeV was required in order to have an acceptable trigger rate. The dynode signals of the Z-counters were processed in 10 Camac ADC's and summed according to the trigger pattern of the event.

The energy response of the calorimeter counters was determined by comparing event by event the positron momentum measured in the streamer chamber (at 3.5 T) with the corresponding calorimeter energy stored on tape (fig. 8). For this purpose the well identifiable positrons from radiative pion capture with subsequent conversion of the photon could be used. The energy calibration was checked with electrons from bound muon decay. For several energies, the calorimeter spectra were simulated by the Monte Carlo method and then compared with the measured spectra. Calculated and measured spectra proved to be in good agreement<sup>42</sup>). Fig.

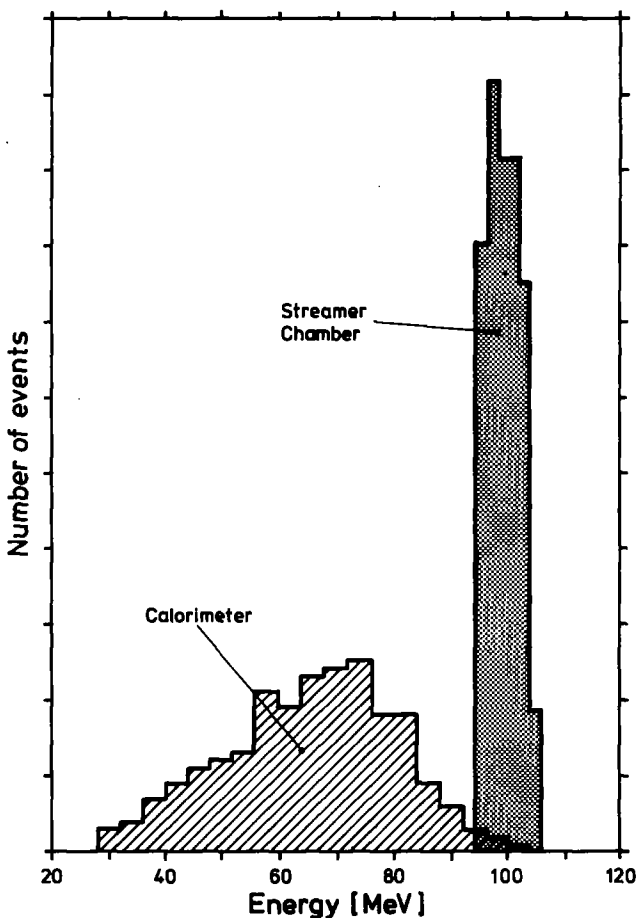


Fig. 8. Calorimeter energy spectrum of positrons with momenta between 94 and 106 MeV/c measured in the streamer chamber.

9 shows the efficiency of the calorimeters as a function of the electron or positron energy.

The energy calibration of the 10 calorimeter counters  $Z_i$  was found to vary as much as 15% with varying beam intensity. In spite of the use of high-rate photomultiplier base circuits with transistor-stabilized dynode voltages, the gain of the photomultipliers began to increase when the anode current rose to typically 15  $\mu\text{A}$  due to the beam. To keep the energy calibration unaffected by changes of the beam intensity, the anode currents of the calorimeter photomultipliers were stabilized at 40  $\mu\text{A}$  by means of light emitting diodes. LED pulses with feedback controlled amplitudes were supplied to each counter  $Z_i$  and improved the gain stability to about 1%. This method of gain stabilization worked well over a wide range of rates (e.g. 5 kHz to 100 kHz) of the LED pulses, but gave poor results for continuous

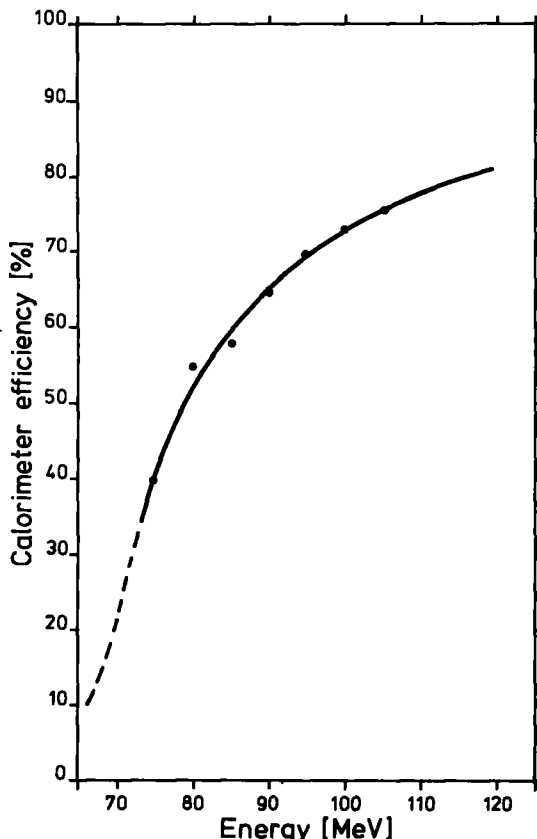


Fig. 9. Calorimeter efficiency as a function of the electron or positron energy measured in the streamer chamber, with the lower discriminator level set at 55 MeV.

illumination of the phototubes by driving the LEDs at dc. We chose a rate of 30 kHz and pulsed the LEDs during beam-on cycles when the apparatus was vetoed.

Gain shifts of the calorimeter photomultipliers were monitored by measuring the spectra of Am light pulsers (NE 130 Light Pulser) installed in every block. The peak position of these spectra, corresponding to an energy deposition of about 30 MeV, could be determined to an accuracy of  $\pm 1\%$ . Within 3 years, the light output of the Am light pulsers decreased by about 10% on the average. It was low enough not to disturb the experiment in any way. An additional system consisting of one central source of light emitting diodes was installed to monitor the gain with the beam on. Light pulses were guided to the photomultipliers through optical fibres and produced signals similar to those of ionizing particles. Spectra of this central light pulser as seen by every photomultiplier were accumulated and compared with standard spectra.

The long-term stability of the detector was checked by measuring the spectrum of throughgoing cosmic ray muons.

## 2.6. TRIGGER LOGICS

**2.6.1. Definition of the trigger.** The aim of the experiment was to measure all electrons and positrons produced in the target during beam-off cycles with a momentum between 80 and 130 MeV/c directed roughly perpendicularly to the beam axis. Such electrons and positrons produced a signal in each of the above-mentioned trigger counter rings X, S and Y as well as in the calorimeter counter ring Z, which allowed a rough energy measurement.

The geometrical correlation between the hit X and Y counters was weak, due to the magnetic field, the accepted energy range, and the emission angle range of the electrons or positrons. It could nevertheless be used to define a trigger condition T:

$$T = K_i Y_i S X_{i \pm l} \bar{A} \bar{B} \bar{D} \bar{E} \quad (i = 1, 2, \dots, 10; l = 1, 2, 3, 4).$$

A is the OR of all anticounters against cosmic ray background,  $\bar{B}$  the beam-off gate and D stands for computer and other dead-times. The analog sum  $K_i$  of the signals from the 3 calorimeter blocks  $Z_{i-1}$ ,  $Z_i$  and  $Z_{i+1}$  closest to the hit Čerenkov counter  $Y_i$  had to be larger than some threshold, which was chosen to be 55 MeV. Finally  $\bar{E}$  is the veto for too energetic events, i.e. events with a total energy deposition larger than 150 MeV in all 10 calorimeter blocks together.

**2.6.2. Trigger electronics.** Fig. 10 shows the block diagram of the trigger electronics. The calorimeter fan-in integrated the fast photomultiplier signals of the 10 counters  $Z_i$  ( $\tau_{\text{int}} = 50$  ns) and generated the above-mentioned 10 "cluster signals"  $K_i$  and also the total sum signal  $\Sigma$  used for the  $\bar{E}$ -veto. The advantages of integrating the calorimeter signals were a less critical timing and sharper energy cuts by means of pulse-height discrimination. The modular construction of the "trigger logic", using mainly ECL 10 000 circuits and patchboard wiring, allowed an easy change of the trigger conditions for test measurements.

**2.6.3. Adjustment of the beam-off gate and measurement of the beam-on to beam-off ratio.** A pick-up signal of the beam pulser electrodes was available for synchronizing the beam-off gate. It was also used to start a clock which measured the arrival time of each event with respect to the beam pulser. This clock consisted of a 50 MHz crystal oscillator, a fast scaler and an appropriate stop and reset logic.

The delay and the width of the beam-off gate were adjusted by measuring the pion plus muon rates behind the streamer chamber both in and out of gate with a special counter telescope. This telescope consisted of a sandwich arrangement of 4 lucite Čerenkov counters ( $10 \times 10 \times 1$  cm $^3$ ) and 3 small plastic scintillation counters ( $12 \times 12 \times 3$  mm $^3$ ). A "telescope trigger" was defined as a coincidence of the 3 scintillation counters with no simultaneous Čerenkov counter signal, vetoing

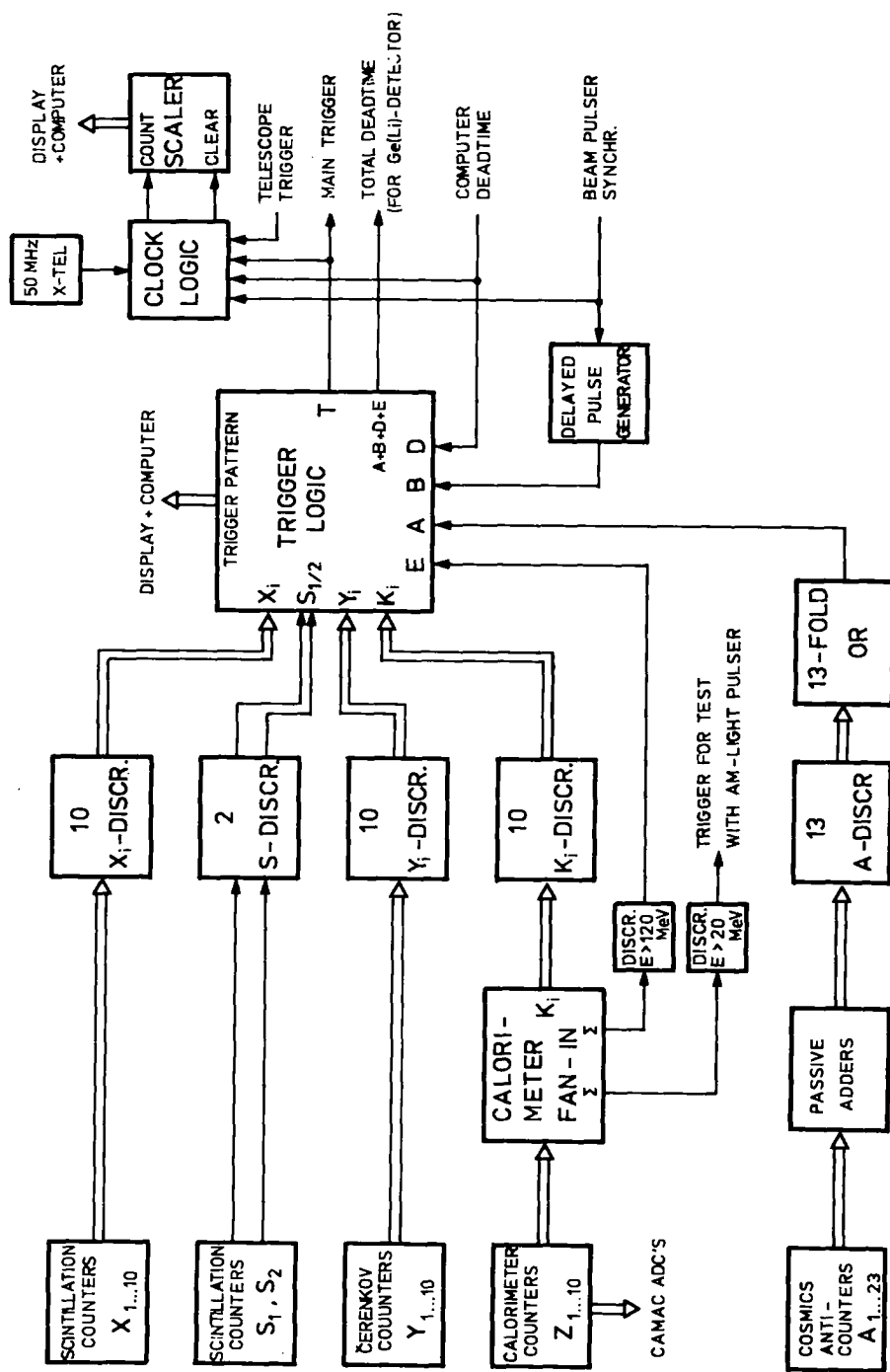


Fig. 10. Simplified block diagram of the trigger electronics.

in this way the delayed electrons from muon decay. The flux of delayed electrons through the 3 scintillation counters during beam-off cycles was about 1% of the flux of pions and muons during beam-on cycles. Therefore the Čerenkov counter veto had to be very efficient, since beam-on to beam-off intensity ratios of the order of  $10^7$  had to be measured. For each telescope trigger within the beam-off gate, the arrival time with respect to the beam pulser was measured with the clock mentioned before, in the same manner as for normal trigger events. The width and the delay of the beam-off gate were set in such a way that about one telescope trigger per second occurred symmetrically at early and late times in the gate (figs. 11a, 11b). The time distribution of the telescope triggers was recorded on tape simultaneously with the normal trigger events. By analysing the time distribution of the telescope triggers, a final adjustment of the accepted beam-off time could be done off-line.

## 2.7. ON-LINE COMPUTING

A Hewlett-Packard minicomputer (HP21MX/M) with a Camac system was used for data taking and for monitoring the experiment. The following data were recorded and written on tape for each trigger event: (i) the energy deposited in the ten calorimeter blocks, (ii) the pattern of all scintillation and Čerenkov counters (this pattern was also displayed on-line with a geometrical lamp arrangement), (iii) the arrival time of each event with respect to the beam pulser, and (iv) the spectrum measured by the Ge(Li) detector since the last event.

Several tests were performed periodically to check the proper operation of the setup. These tests, which were done simultaneously with the recording of event data, included:

(i) Tests of the calorimeters: pulses were sent both to the ADC's to check their conversion stability and to the calorimeter LEDs to check the gain of the phototubes. During beam-off cycles, americium spectra were taken to test the stability of the LED pulser, and cosmic-ray spectra were measured to check the long-term stability of the Am lamps.

(ii) Tests of the other trigger counters: the trigger patterns of the events were accumulated and used to test the symmetrical operation of the ring detector. Single counting rates were checked.

(iii) Test of the streamer chamber: the delay time and the height of the high-voltage pulses were monitored.

## 2.8. Ge(Li) DETECTOR

To determine the total number of muons captured by sulfur nuclei during the measuring time, we used a single open-ended Ge(Li) detector (Philips APY 43) with a useful volume of  $43 \text{ cm}^3$ . It was placed 110 cm from the target, behind two

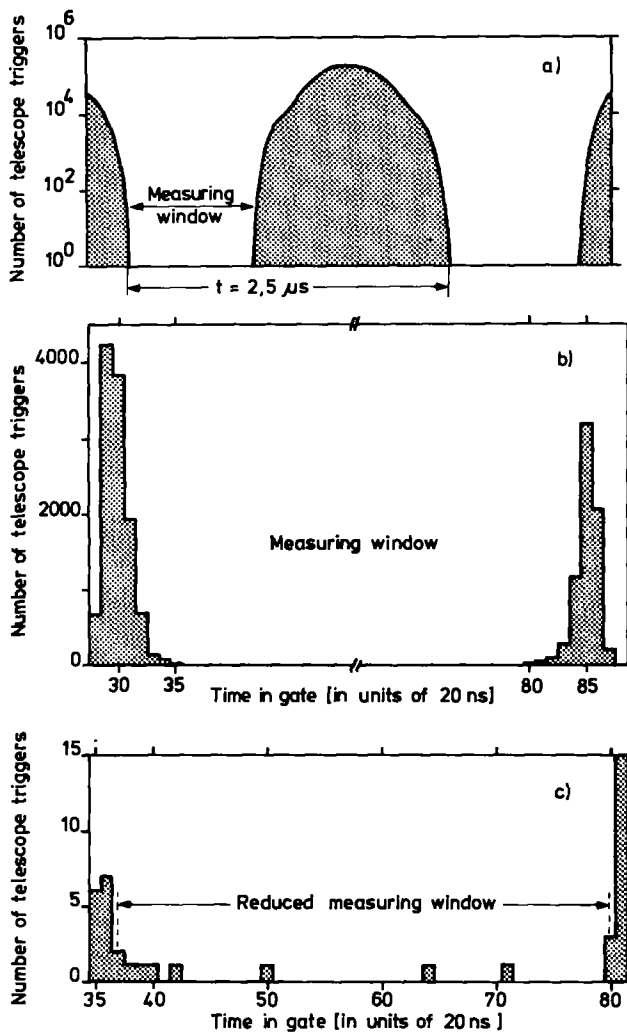


Fig. 11. Beam suppression measured by the time distribution of the telescope triggers. For each run, a reduced evaluation window within the measuring window was set off-line by requiring a beam suppression of  $10^7$ .

slightly excavated calorimeter blocks (figs. 2, 3). To determine the number of captured muons, the number of photons produced in some specific final state of nuclear muon capture had to be measured. The final state of  $\mu^- + ^{32}\text{S} \rightarrow \nu_\mu + n + ^{31}\text{P}^*$ , followed by  $^{31}\text{P}^* \rightarrow ^{31}\text{P} + \gamma$ , fulfilled two important requirements. First, the photon energy  $E_\gamma = 1266.1 \text{ keV}$  was appropriate for the Ge(Li) detector, i.e. small enough to guarantee a reasonable efficiency, and large enough to keep the background sufficiently low. This was important, since every event seen by the Ge(Li) detector

in a given energy window caused a computer interrupt and therewith a deadtime of the whole setup of some 100  $\mu\text{s}$ . The second condition fulfilled by the selected final state was its high photon yield  $Y$  (number of photons per nuclear muon capture). It was measured in a separate run by comparing directly the number of 1266.1 keV photons from  $^{31}\text{P}^*$  decay with the number of 516 keV photons from the cascading muon ( $K_\alpha$  line in sulfur). Using the known data for the capture probability of muons in sulfur<sup>43</sup>) and the yield of the sulfur  $K_\alpha$  line<sup>44</sup>), a  $\gamma$ -yield of  $Y = (22 \pm 2)\%$  was obtained.

For an accurate analysis of the 1266.1 keV peak area, it was essential to have continuous control over the shape of the peak, which was affected in the course of long running periods by electronics drifts as well as by particles hitting the detector, and which had to be separated from several background peaks. The specific peak shape for each run was taken from the isolated  $^{41}\text{Ar}$  background peak at 1293.3 keV. After subtracting the background, the number  $N_0$  of counts within the 1266.1 keV peak area could be determined to an accuracy of  $\pm 10\%$ . The peak area typically amounted to 10–20% of the background beneath it. Taking into account both the  $\gamma$ -yield  $Y$  mentioned before and the total efficiency  $\epsilon$ , the number of captured muons could be calculated from  $N_c = N_0 / Y\epsilon$ . The total efficiency  $\epsilon = (3.6 \pm 0.2) \times 10^{-6}$  was the product of the solid-angle factor  $\Omega/4\pi \approx 0.027\%$ , the Ge(Li) efficiency  $\epsilon_{\text{abs}} \approx 6.4\%$  at 1266.1 keV, and the transmission probability  $T$  for a 1266.1 keV photon from the target. The product of  $\epsilon_{\text{abs}}$  and  $\Omega$  was measured for several energies with calibrated  $\gamma$  sources and interpolated to 1266.1 keV, whereas the absorption in the target ( $1 - T$ ) was calculated by a Monte Carlo program. The total error  $\Delta N_c$ , given by the individual errors of  $N_0$ ,  $Y$  and  $\epsilon$ , and a timing error of about 10% (accuracy  $\pm 50$  ns), was of the order of 20%.

For the whole experiment, the total number of captured muons was found to be  $N_c^- = 6.7 \times 10^{11}$  for the  $\mu^- \rightarrow e^-$  experiment and  $N_c^+ = 5.9 \times 10^{11}$  for the  $\mu^- \rightarrow e^+$  experiment (for a short period we searched exclusively for  $\mu^- \rightarrow e^-$  conversion).

## 2.9. RECONSTRUCTION OF TRACKS

The streamer chamber pictures were all carefully scanned, and about 1 out of 10 pictures turned out to contain a clear electron or positron track. Tracks of interest were digitized together with fiducial marks by means of a Tektronix graphics tablet on a HP minicomputer. Using geometrical reconstruction programs, a three-dimensional reconstruction of the tracks was possible after eliminating the distortions caused by the image intensifier tubes. These distortions were corrected by means of the periodically photographed reference grid, which was digitized in the same way as the tracks and the fiducial marks.

Momenta could be determined to an accuracy of 3% at 100 MeV/c. This precision was checked by measuring the electron spectrum from  $\pi^+ \rightarrow e^+ \nu_e$  decays at a magnetic field of  $B = (70/100) \times 3.5 \text{ T} = 2.45 \text{ T}$ .

### 3. Background

In this section, we discuss the background processes to the hypothetical  $\mu^- \rightarrow e^-$  and  $\mu^- \rightarrow e^+$  conversion. Simulated conversion and background spectra are presented and compared with the measured spectra. Details of the simulation calculations are treated in sect. 4.

As mentioned before (subsect. 2.1), electrons from  $\mu^- \rightarrow e^-$  conversion are expected to be emitted monoenergetically, whereas positrons from  $\mu^- \rightarrow e^+$  conversion should have a wide spectrum of energies due to the excitation of the nucleus involved. The expected spectra of conversion electrons and positrons were simulated, taking into account the energy loss in the target and the momentum resolution of the streamer chamber. In the case of  $\mu^- \rightarrow e^+$  conversion, a lorentzian distribution (mean  $E^*$ , width  $\Gamma$ ) of the nuclear excitation energies  $E^*$  was assumed. Figs 12 and 13 show simulated  $\mu^- \rightarrow e^-$  and  $\mu^- \rightarrow e^+$  spectra for hypothetical conversion branching ratios of  $10^{-9}$  and  $10^{-8}$  (with  $E^* = \Gamma = 20$  MeV), respectively. Comparing these spectra with the background spectra (see below), the momentum ranges 96–112 MeV/c for electrons and 90–112 MeV/c for positrons were selected for the search of  $\mu^- \rightarrow e^\pm$  conversion.

The following background processes producing single electrons or positrons with an energy of about 100 MeV had to be considered:

- (i) beam correlated background (radiative pion capture, fast neutrons),
- (ii) background from stopped muons (bound muon decay, radiative muon capture),
- (iii) background from cosmic rays, and
- (iv) accidental background.

#### 3.1. BEAM CORRELATED BACKGROUND

**3.1.1. Radiative pion capture.** About 30% of the particles stopped in the target were pions. Once captured by the sulfur nuclei, 1.7% of these pions gave rise to the emission of a photon<sup>45)</sup> through radiative pion capture  $\pi^- + ^{32}\text{S} \rightarrow \gamma + \dots$ . The energy distribution of these photons<sup>45)</sup> extends from 0 to 140 MeV, with a broad maximum between 100 and 140 MeV. With a continuous beam, these photons would have led to a disastrous background of 100 MeV electrons and positrons (through Compton scattering or conversion into an asymmetric  $e^+e^-$  pair). By the use of a pulsed beam, this background could be efficiently suppressed. Data were taken only during beam-off cycles, and only those taken within a further reduced beam-off gate were analysed. This reduced beam-off gate was set off-line by requiring the ratio of telescope triggers within the reduced gate to all telescope triggers to be  $10^{-7}$  (subsect. 2.6.3).

To estimate the expected number of background events from radiative pion capture, the number of electrons and positrons in the selected momentum range

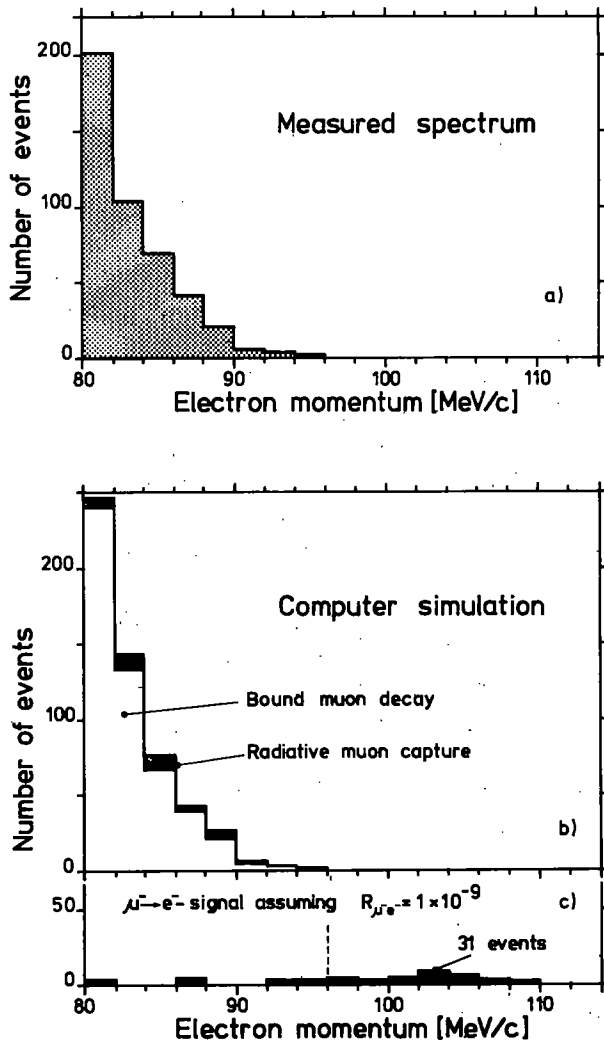


Fig. 12. (a) Measured electron spectrum. (b) Monte Carlo simulated background spectrum from bound muon decay and radiative muon capture. (c) Monte Carlo simulated spectrum of  $\mu^- \rightarrow e^-$  conversion electrons, assuming a conversion branching ratio of  $R_{\mu^-e^-} = 10^{-9}$ , and monoenergetic conversion electrons at 104.7 MeV.

relative to the total number of telescope triggers was measured in a special run with a continuous beam.

**3.1.2. Fast neutrons.** Fast neutrons from material hit by the primary beam could produce pions in the detector material. Photons either from  $\pi^0$  decays or from radiative pion capture could then give rise to background events through Compton scattering or conversion. This background was strongly suppressed by shielding the area with heavy concrete, and by pulsing also the ion source of the accelerator, so

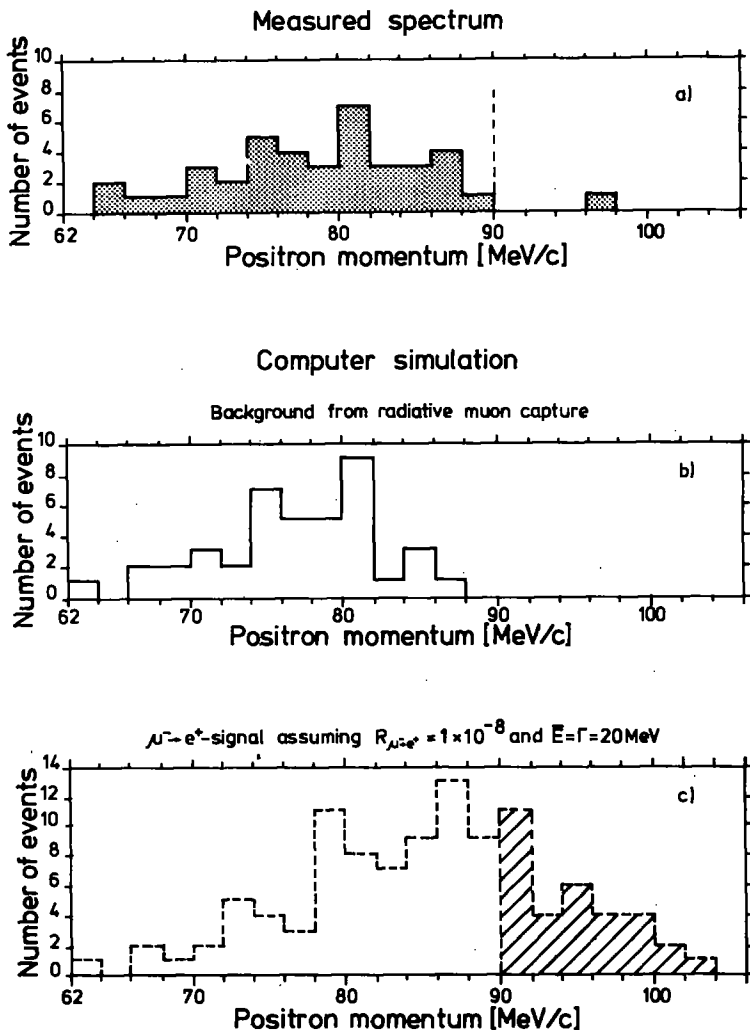


Fig. 13. (a) Measured positron spectrum. (b) Monte Carlo simulated background spectrum from radiative muon capture. (c) Monte Carlo simulated spectrum of  $\mu^- \rightarrow e^+$  conversion positrons, assuming a conversion branching ratio of  $R_{\mu^- e^+} = 10^{-8}$  and a lorentzian distribution of excitation energies with a mean of 20 MeV and a width of 20 MeV.

that the intensity of the deflected beam getting onto the beam-stop during beam-off cycles could be reduced to a few percent of the full intensity.

### 3.2. BACKGROUND FROM STOPPED MUONS

A stopped muon, trapped in the Coulomb field of a sulfur nucleus, cascades instantly down to its lowest orbit, from where it

- (i) is captured by the sulfur nucleus and converted into a neutrino with a probability<sup>43,46)</sup> of about 75% ( $\mu^- + {}^{32}\text{S} \rightarrow \nu_\mu + \dots$ ), or
- (ii) decays with a probability of about 25% (bound muon decay), or
- (iii) induces radiative muon capture ( $\mu^- + {}^{32}\text{S} \rightarrow \nu_\mu + \gamma + {}^{32}\text{P}^*$ ) with a probability of the order of<sup>46)</sup>  $10^{-4}$ , or
- (iv) is hypothetically converted into an electron or positron.

Searching for the so-far unobserved conversion processes (iv), the processes (ii) and (iii) were unavoidable sources of background.

**3.2.1. Bound muon decay.** Electrons from bound muon decay in sulfur can have energies up to the maximum of 104.7 MeV, the energy of the conversion electrons searched for. Using the theoretical energy spectrum<sup>47)</sup> of electrons from bound muon decay in sulfur, a Monte Carlo simulation of the expected momentum spectrum was performed (fig. 12b). This background is absent for  $\mu^- \rightarrow e^+$  conversion.

**3.2.2. Radiative muon capture.** The second inherent background process is radiative muon capture with subsequent conversion of the photon into an asymmetric  $e^+e^-$  pair. Additional electrons are produced by Compton scattering of the photons in the target. The photon spectrum averaged over all possible nuclear final states had to be taken from experiment. Since no data were available for sulfur, we used the experimentally well-known<sup>48)</sup> photon spectrum of  ${}^{40}\text{Ca}$ , which extends up to 86.5 MeV. The photon spectra of other medium-weight nuclei such as sulfur are expected to be not very different from this spectrum. The resulting simulated background spectra are shown in figs. 12b and 13b.

### **3.3. BACKGROUND FROM COSMIC RAYS**

In addition to the ring anticounters, the whole setup was shielded with a roof of scintillation anticounters against cosmic-ray muons. By means of this roof, both the trigger rate and the number of events with faked tracks coming from the target could be considerably reduced.

In the off-line analysis, two efficient conditions served to eliminate further cosmic-ray events. The first condition required the total energy deposited in the calorimeter to be less than 95 MeV, since  $\frac{2}{3}$  of the cosmic-ray muons passing through two calorimeter blocks deposited more than 100 MeV. The resulting efficiency loss for good events was less than 1%. The second condition was used to eliminate events from cosmic-ray muons entering or leaving the streamer chamber near the target, simulating thereby a track coming from the target. This condition made use of the fact that the X-counters, which closely surrounded the streamer chamber, had been extended 4 cm beyond each side of the chamber: it required all events with two X-counters fired on opposite halves of the ring-detector to be rejected. Cosmic-ray neutrons could induce background events in the same way as the beam

correlated neutrons discussed before. The flux of these neutrons was reduced by a factor of about 200 by shielding the whole area with a 1.5 m thick iron roof.

### 3.4. ACCIDENTAL BACKGROUND

Only 13% of the triggers were correlated to a visible track from the target. Most triggers were caused by scattered muons which did not stop in the target. Since the chamber was operated with a memory time of 800 ns, an old track produced in the preceding beam-on cycle could accidentally be in agreement with the given trigger pattern. In addition, pions stopping in the target produced a lot of strongly ionizing protons, part of which looked like minimum ionizing particles in the following beam-off cycle and could therefore be mistaken for positrons. Comparing the rate of accidental tracks with a correct trigger pattern to the rate of those with an incorrect trigger pattern, it was found that this accidental background was negligible for  $\mu^- \rightarrow e^-$  conversion. For  $\mu^- \rightarrow e^+$  conversion it turned out to be the main source of background.

### 3.5. TOTAL BACKGROUND

The measured electron spectrum is shown in fig. 12a. It agrees well with the combined background spectrum expected from bound muon decay and radiative muon capture (fig. 12b). The number of measured events above 80 MeV/c differs by about 20% from the number of events expected from the simulation calculations. This difference may be attributed to the experimental uncertainty in the number of captured muons. The measured background spectrum extends up to 96 MeV/c. For this reason the momentum range 96–112 MeV/c was chosen for the search of conversion electrons. About 80% of the conversion electrons were expected in this interval; the loss of 20% is mainly due to the bremsstrahlung of the electrons in the target. One background event was expected in the selected range, none was found.

The measured positron spectrum is shown in fig. 13a. Below 90 MeV/c, it is in good agreement with the background spectrum expected from radiative muon capture (fig. 13b). Conversion positrons were searched for above 90 MeV/c. In this momentum range we found one event (at 98 MeV/c), to be compared with an expected background of  $3 \pm 1$  (mainly accidentals).

## 4. Monte Carlo simulation of the experiment

In the following we report on the Monte Carlo simulation calculations, the results of which have already been presented in the previous section. These calculations were carried out to get information on

- (i) the dependence of the detector acceptance on the initial electron (positron) energy and on the magnetic field in the streamer chamber, taking into account the correct trigger condition,
- (ii) the spectra expected from  $\mu^- \rightarrow \text{e}^-$  conversion electrons and from  $\mu^- \rightarrow \text{e}^+$  conversion positrons,
- (iii) the background spectra expected from bound muon decay and radiative muon capture.

#### 4.1. SIMULATION PROCEDURE

A first version of the simulation program was written in the planning stage of the experiment to optimize both the design of the double coil and the shape and size of the target for a maximum muon stop rate. A complete simulation of the trajectories of electrons and positrons, taking into account energy losses and multiple scattering in different parts of the system, was done later on for the final analysis of the data.

The correct trigger condition could only be checked by simulating the entire trajectory of a particle from the target to the calorimeter. For electrons and positrons with energies around 100 MeV, this very time-consuming simulation could however be avoided using a simplified trigger condition. The  $\mu^- \rightarrow \text{e}^-$  and  $\mu^- \rightarrow \text{e}^+$  conversion spectra as well as the background spectra were not affected thereby. With this simplified trigger condition, each particle was either rejected or accepted with a constant efficiency. A particle was accepted, if its position and direction at the starting point in the target fulfilled a simple geometrical condition, and if its energy exceeded a critical energy depending on the magnetic field and the initial conditions of the particle. An approximate but simple formula for this critical energy was developed by studying a sample of full trajectories in the magnetic field.

The simulation procedure was subdivided as follows: First, the starting point of an electron or positron (=position of the stopped muon) was homogeneously distributed in the given hollow-cylindrical target. The details of this distribution were unimportant because of the energy losses in the target. Then a starting direction was chosen isotropically within a solid angle large enough to cover the region defined by the simplified trigger condition. After choosing the electron (positron) energy according to the given distribution, energy losses and multiple scattering were applied according to the remaining pathlength in the target. In order to account for the straggling of the energy loss, a fast routine was written based on a distribution of the radiation loss given by Heitler<sup>49</sup>). The distribution of the multiple-scattering angle was assumed to be gaussian with a variance depending on the electron (positron) energy and the radiation length of the target material. Whenever the geometrical and magnetic trigger condition were both satisfied, the energy of the electron (positron) was finally changed according to a gaussian experimental error and filled into a histogram.

The initial energy of electrons from  $\mu^- \text{S} \rightarrow \text{e}^- \text{S}$  was assumed to be

$$E_- = m_\mu (1 - \frac{1}{2}(Z\alpha)^2) - m_\mu^2/2M = 104.7 \text{ MeV},$$

where both the binding energy of the muon and the recoil energy of the nucleus of mass  $M$  have been taken into account. The initial energy of positrons from  $\mu^- \text{S} \rightarrow \text{e}^+ + \dots$  is given by

$$E_+ = E_- + M(A, Z) - M(A, Z-2) - E^* = 101.8 \text{ MeV} - E^*.$$

Here  $M(A, Z)$  is the mass of the nucleus with mass number  $A$  and atomic number  $Z$ .  $E^*$  is the unknown excitation energy of the nucleus in the final state. In the simulation, the distribution of  $E^*$  was assumed to be lorentzian, with given mean value and width. The initial energy distribution of the background electrons and positrons are discussed in subsect. 4.2.

For a total number  $N_c$  of nuclear muon captures in the beam-off gate and a given  $\mu \rightarrow \text{e}$  branching ratio  $R_{\mu e}$ , the number of conversion electrons (positrons) is  $N = R_{\mu e} N_c$ . Using the measured<sup>43)</sup> mean lifetime  $\tau = 558 \text{ ns}$  of muons in sulfur gives the total number of bound muon decays:  $N_d = \tau/(\tau_\mu - \tau) N_c = 0.34 N_c$  ( $\tau_\mu$  = free muon lifetime). Energy-independent reduction factors such as inefficiencies of trigger counters and loss of streamer chamber pictures were directly applied to the total numbers  $N_c$  and  $N_d$ . A substantial energy dependent reduction factor was the inefficiency of the calorimeters, which was determined experimentally (fig. 9).

#### 4.2. ENERGY DISTRIBUTION OF THE BACKGROUND PROCESSES

To calculate the background spectra and to study their dependence on the target material, it was essential to have reliable expressions for the energy spectra both of electrons from bound muon decay and of photons from radiative muon capture for different elements.

**4.2.1. Bound muon decay.** When this work was started, the most complete numerical calculation of the energy spectrum of electrons from bound muon decay, especially near its upper end for the elements O, Si and Cu was the one by Hänggi<sup>50)</sup>. To get the energy spectrum  $N(Z, E) \text{ d}E$  for an element with atomic number  $Z$  we defined a correction factor  $F(Z, E)$  by

$$N(Z, E) = F(Z, E) N_{\text{Born}}(Z, E),$$

where  $N_{\text{Born}}(Z, E)$  is the Born approximation with nuclear recoils taken into account. The high-energy tail of  $N_{\text{Born}}(Z, E)$  can be written as<sup>50)</sup>

$$N_{\text{Born}}(Z, E) \text{ d}E = \frac{256}{\pi} (Z\alpha)^5 E^2 \text{ d}E \int_{p_1}^{p_2} p \frac{A}{(c^2 + p^2)^4} \text{ d}p,$$

where

$$\begin{aligned} A &= (W(3W - 4E) - p^2)(B + p) + (W - 2E)(B^2 - p^2), \\ B &= [W_0(W_0 - 2E) - p^2(1 + 2a(W_0 - E))] / 2E, \\ p_1 &= (E - D) / (1 + 2a(W_0 - E)), \quad p_2 = (E + D) / (1 + 2a(W_0 - E)), \\ D^2 &= (W_0 - E)(W_0 - E + 2aW_0(W_0 - 2E)), \quad a = 1/2M, \quad c = Zam_\mu, \\ W &= W_0 - ap^2, \quad W_0 = m_\mu(1 - \frac{1}{2}(Z\alpha)^2), \end{aligned}$$

$M$  being the mass of the nucleus,  $m_\mu$  the muon mass and  $\alpha = \frac{1}{137}$ . The electron mass was neglected. The upper end of the spectrum is given in a good approximation by

$$E_{\max} = W_0 - aW_0^2.$$

The last term in this expression is the maximal recoil energy transferred to the nucleus. Comparing the Born approximation with the exact spectrum for the elements O, Si and Cu the following simple parametrization of the correction factor was found empirically:

$$F(Z, E) = \exp(-1.24\sqrt{Z}(E/m_\mu - 0.46)).$$

The exact spectra are reproduced with an uncertainty of about 15% for  $E > 50$  MeV.

In the meantime the exact spectrum for our target element sulfur has been calculated by Herzog<sup>42,47</sup>). The present calculation with the correction factor reproduces it with a maximal error of 30%.

To use the above energy distribution for the Monte Carlo simulation of the electron spectrum from bound muon decay, the integral

$$P(E) = \int_E^{E_{\max}} N(Z, E) dE$$

had to be calculated. It represents the probability (per bound muon decay) that the energy of a decay electron exceeds the value  $E$ .  $P(E_i)$  was calculated using Simpson's rule for a given set of energies  $E_i$  sufficiently dense in the energy region of interest.

**4.2.2. Radiative muon capture.** Another source of background electrons as well as positrons is radiative nuclear muon capture with subsequent internal or external conversion of the photon into an asymmetric electron-positron pair. Obviously the electron and positron energy spectra are identical. In the following we discuss the electron spectrum, to which we have to add a contribution due to Compton scattering of the photons (see below).

The probability  $P_1(u, v)$  per  $\mu$ -capture to produce an electron with energy  $E_- \geq u$  and a positron with energy  $E_+ \leq v$  can be written as

$$P_1(u, v) = \int_{u+m_e}^{E_{\max}} W(E_\gamma) \left\{ \int_u^{E_\gamma - m_e} \left[ \phi_1(E_\gamma, E_-) + \frac{x}{l_0} \phi_2(E_\gamma, E_-) \right] \right. \\ \left. \times \theta(E_- + v - E_\gamma) dE_- \right\} dE_\gamma.$$

Here  $W(E_\gamma)$  is the probability density of the photons (per nuclear muon capture);  $\theta$  is the step function, which takes care of the condition  $E_+ = E_\gamma - E_- \leq v$ ;  $x$  is the potential pathlength of a photon in the target (to be compared with the radiation length  $l_0$ );  $\phi_1(E_\gamma, E_-) dE_-$  is the probability that a photon of energy  $E_\gamma$  undergoes internal conversion and yields an electron in the energy interval  $[E_-, E_- + dE_-]$ , and  $(x/l_0)\phi_2(E_\gamma, E_-) dE_-$  is the corresponding expression for an external conversion. The probability density  $\phi_1$  can be determined according to Kroll and Wada<sup>51</sup>). In our case, the external conversion was found to dominate on the average by about one order of magnitude over the internal conversion. For  $\phi_1$ , the following approximation was sufficient:

$$\phi_1(E_\gamma, E_-) \approx 10^{-2} \phi_2(E_\gamma, E_-),$$

where the function  $\phi_2$  is given by<sup>52</sup>)

$$\phi_2(E_\gamma, E_-) = \frac{E_\gamma^2 - \frac{4}{3}E_+E_-}{5E_\gamma^3} \left( \log \left( \frac{2E_+E_-}{E_\gamma m_e} \right) - \frac{1}{2} \right) f(\xi_+),$$

with

$$E_\gamma = E_+ + E_-,$$

$$f(\xi_+) = \frac{2\pi\xi_+}{e^{2\pi\xi_+} - 1}, \quad \xi_+ = \frac{Zam_e}{p_+},$$

$p_+$  = positron momentum.

The contribution of the Compton scattering to the integrated energy distribution of the electrons can be written approximately as

$$P_2(u) = C \int_u^{E_{\max}} W(E_\gamma) \frac{m_e}{E_\gamma} \log \left( 1 + \frac{2}{m_e} (E_\gamma - u) \right) dE_\gamma,$$

with

$$C = 0.15xZ/A, \quad x \text{ in g/cm}^2.$$

The spectrum  $W(E_\gamma)$  is best known experimentally<sup>48,53</sup>) for the nucleus  $^{40}\text{Ca}$ . As it is not expected to be very different for other medium-weight nuclei, we used the  $^{40}\text{Ca}$  photon spectrum given by Hart *et al.*<sup>48</sup>) with the same mean excitation energy of 12.6 MeV for sulfur. The probabilities  $P_1(E_i, v)$  and  $P_2(E_i)$  per nuclear

muon capture to get an electron energy  $E_- > E_i$  and a positron energy  $E_+ < v$  were then calculated by Simpson's rule.  $P_1$  is not very sensitive to the maximum positron energy  $v$ , which was chosen to be 8 MeV because positrons with energies below this limit were hardly recognized on the streamer chamber pictures. In the energy interval  $E_{\max} - 5$  MeV to  $E_{\max}$  Compton scattering in sulfur contributes about the same number of electrons as conversion. For lower energies Compton scattering becomes less important. The energy loss of an electron in the target was calculated from its pathlength, which on the average is  $\frac{1}{2}x$  for a photon of potential pathlength  $x$ .

## 5. Results

### 5.1. MUON-ELECTRON CONVERSION

The electron momentum spectrum measured in the search of  $\mu^- + {}^{32}\text{S} \rightarrow e^- + {}^{32}\text{S}$  is shown in fig. 12a. This spectrum, which is the result of a total of  $N_c^- = 6.7 \times 10^{11}$  muons captured by sulfur nuclei, is entirely compatible with the combined background spectrum expected from bound muon decay and radiative muon capture (fig. 12b). No  $\mu^- \rightarrow e^-$  candidate event was found in the momentum range 96–112 MeV/c chosen for the evaluation. The expected background in this range was one event. The upper bound  $N_\alpha$  on the number of expected  $\mu^- \rightarrow e^-$  events at the  $\alpha = 0.90$  confidence level can be calculated from the number  $n$  of observed candidate events and the mean value  $\bar{B}$  of the expected background with the formula

$$\frac{\int_0^{N_\alpha} P_n(\bar{B} + N) dN}{\int_0^\infty P_n(\bar{B} + N) dN} = \alpha,$$

where  $P_n(m)$  is the Poisson distribution with mean value  $m$ . With  $n = 0$  and  $\bar{B} = 1$  we find  $N_{\alpha=0.9} = 2.3$ . From this number the 90% CL upper limit on the branching ratio of  $\mu^- + {}^{32}\text{S} \rightarrow e^- + {}^{32}\text{S}$  relative to ordinary muon capture can be derived:

$$R_{\mu^- e^- ({}^{32}\text{S})} = \frac{\Gamma(\mu^- + {}^{32}\text{S} \rightarrow e^- + {}^{32}\text{S})}{\Gamma(\mu^- + {}^{32}\text{S} \rightarrow \nu_\mu + \dots)} < \frac{2.3}{N_c^- e^-} \quad (90\% \text{ CL}).$$

The total efficiency  $\epsilon^-$  is given by  $\epsilon^- = \epsilon_T \epsilon_F \epsilon_A^-$ , where  $\epsilon_T = 0.9$  is the efficiency of the trigger counters (without calorimeters) for minimum ionizing particles,  $\epsilon_F = 0.85$  is the fraction of pictures which could be analysed, and  $\epsilon_A^- = 0.06$  is the acceptance for electrons from  $\mu^- + {}^{32}\text{S} \rightarrow e^- + {}^{32}\text{S}$ . The factor  $\epsilon_A^-$  takes into account the detector geometry, the magnetic field, the energy losses in the various detector parts, the calorimeter efficiency, and the probability of a  $\mu^- \rightarrow e^-$  electron to fall into the selected momentum range 96–112 MeV/c. The actual value of  $\epsilon_A^-$  was calculated

as described in sect. 4. Finally we recall our assumption that the coherent part of the  $\mu^- \rightarrow e^-$  conversion is 100% (see sect. 2.1). With these numbers the total efficiency is  $\varepsilon^- = 0.046$ , and we get the upper limit

$$R_{\mu^-e^-}(^{32}\text{S}) < 7 \times 10^{-11} \quad (90\% \text{ CL}).$$

This limit is more than two orders of magnitude below that one given in ref.<sup>12)</sup> for copper.

The experimental error (due to uncertainties in  $N_c^+$  and  $\varepsilon_A^+$ ) is estimated to be less than 25% and is not included in the confidence level.

## 5.2. MUON-POSITRON CONVERSION

The positron spectrum measured in the search of  $\mu^- + ^{32}\text{S} \rightarrow e^+ + ^{32}\text{Si}^*$  is shown in fig. 13a. This spectrum, which corresponds to a total of  $N_c^+ = 5.9 \times 10^{11}$  muons captured by sulfur nuclei, agrees well with the background spectrum expected from radiative muon capture (fig. 13b). One candidate event ( $n = 1$ ) was found between 90 and 112 MeV/c, which was the momentum range chosen for the evaluation in this case. The expected background in this interval was  $\bar{B} = 3$  events. With the formula given in subsect. 5.1, the upper limit  $N_\alpha$  on the expected number of  $\mu^- \rightarrow e^+$  events at the  $\alpha = 0.90$  confidence level is found to be  $N_\alpha = 2.9$ , resulting in the following 90% CL upper limit on the branching ratio of  $\mu^- + ^{32}\text{S} \rightarrow e^+ + ^{32}\text{Si}^*$  relative to ordinary muon capture:

$$R_{\mu^-e^+}(^{32}\text{S}) = \frac{\Gamma(\mu^- + ^{32}\text{S} \rightarrow e^+ + ^{32}\text{Si}^*)}{\Gamma(\mu^- + ^{32}\text{S} \rightarrow \nu_\mu + \dots)} < \frac{2.9}{N_c^+ \varepsilon^+} \quad (90\% \text{ CL}).$$

The total efficiency  $\varepsilon^+$  can again be written as  $\varepsilon^+ = \varepsilon_T \varepsilon_F \varepsilon_A^+$  with the same  $\varepsilon_T$  and  $\varepsilon_F$  as in subsect. 5.1. For a lorentzian distribution of the excitation energies  $E^*$  with  $\bar{E}^* = \Gamma = 20$  MeV, the Monte Carlo calculated acceptance  $\varepsilon_A^+$  for positrons generated in the momentum range 90–112 MeV/c was  $\varepsilon_A^+ = 0.0075$ . With the ensuing total efficiency  $\varepsilon^+ = 0.0057$  we find

$$R_{\mu^-e^+}(^{32}\text{S}) < 9 \times 10^{-10} \quad (90\% \text{ CL}).$$

Again the experimental error due to uncertainties in  $N_c^+$  and  $\varepsilon_A^+$  is not included in the 90% confidence level. It is estimated to be less than 25%.

Since the upper limit on  $R_{\mu^-e^+}$  depends sensitively on the assumptions made on the nuclear excitation, we present in table 1 a list of limits obtained (i) for a lorentzian distribution of the excitation energies and different values of the parameter  $\bar{E}^*$  (with  $\Gamma = \bar{E}^*$ ), and (ii) for a  $\delta$ -distribution of the excitation energies. The corresponding acceptances  $\varepsilon_A^+$  are also shown.

Based on the arguments given at the beginning (subsect. 2.1), we consider a mean excitation energy somewhat above that one of ordinary muon capture to be a reasonable assumption and regard the above-mentioned upper limit for  $\bar{E}^* = \Gamma =$

TABLE 1

Upper limits on  $R_{\mu^- \text{e}^+}({}^{32}\text{S})$  for lorentzian distributions of the nuclear excitation energies  $E^*$ , for different mean values  $\bar{E}^*$  and widths  $\Gamma$

Distribution of excitation energies $E^*$	$\bar{E}^*$ (MeV)	$e_A^+$ (%)	Upper limit on $10^{10} \times R_{\mu^- \text{e}^+}({}^{32}\text{S})$ (90% CL)	Remarks
lorentzian with $\Gamma = \bar{E}^*$	0	7.34	0.9	quasielastic
	5	4.84	1	
	10	2.49	3	
	15	1.20	5	
	20	0.75	9	medium excited
	25	0.55	12	highly excited
	30	0.43	15	
	35	0.35	18	
	40	0.29	22	
	0	7.34	0.9	
$\delta$ -function	5	6.09	1	
	10	2.49	3	
	15	0.15	43	
	20	0.00	—	

The corresponding apparatus acceptances  $e_A^+$  (defined in the text) are also shown.

20 MeV as our final result. This limit is more than an order of magnitude below the limit for copper given in ref. <sup>12)</sup>.

In a recent experiment <sup>54)</sup>, an upper bound has been established on  $\mu^- + {}^{127}\text{I} \rightarrow \text{e}^+ + {}^{127}\text{Sb}^*$  relative to ordinary muon capture by searching for the  ${}^{127}\text{Sb}^*$  nuclei in the final state. This bound can be written as  $R_{\mu^- \text{e}^+}({}^{127}\text{I}) < 3 \times 10^{-10}/P$ , where  $P$  is the probability that the conversion process leads to a  ${}^{127}\text{Sb}^*$  nucleus in the final state (no break-up of the nucleus). Since  $P$  is unknown, no new upper limit for  $\mu^- \rightarrow \text{e}^+$  conversion on  ${}^{127}\text{I}$  can be derived from this result, as misleadingly indicated in the title of ref. <sup>54)</sup>. In view of the measured <sup>55)</sup> probability of about 92% for nucleon emission in ordinary muon capture by  ${}^{127}\text{I}$ , we expect  $P$  to be not larger than a few percent.

## 6. Discussion

### 6.1. MUON-ELECTRON CONVERSION

**6.1.1. Phenomenological approach.** In the pioneering work of Feinberg and Weinberg <sup>2)</sup>, muon-electron conversion was treated as a process occurring through the exchange of a virtual photon. In this case the conversion branching ratio relative to ordinary muon capture can be expressed by four electromagnetic form factors corresponding to E0, M0, E1 and M1 transitions. Nonphotonic contributions can

be included by defining<sup>24)</sup> generalized “effective” form factors  $f_{M0}^{\text{eff}}(q^2)$ ,  $f_{E1}^{\text{eff}}(q^2)$ ,  $f_{M1}^{\text{eff}}(q^2)$  and  $f_{E0}^{\text{eff}}(q^2)$ . In specific gauge theories of the weak and electromagnetic interactions, these form factors are finite and calculable. From the upper limit on  $R_{\mu^-e^-}(^{32}\text{S})$  we find:

$$|f_{E0}^{\text{eff}}(-m_\mu^2) + f_{M1}^{\text{eff}}(-m_\mu^2)|^2 + |f_{E1}^{\text{eff}}(-m_\mu^2) + f_{M0}^{\text{eff}}(-m_\mu^2)|^2 < 2 \times 10^{-23}.$$

A more accurate analysis of muon-electron conversion, which includes nonphotonic contributions from the beginning, was given by Shanker<sup>56)</sup>. The branching ratio for muon-electron conversion is expressed in terms of phenomenological coupling constants  $g_V^{(0)}$  and  $g_V^{(1)}$ , which determine the strength of the coupling between the ( $\mu e$ ) current and the isoscalar or isovector quark (vector) currents (relative to the ordinary weak coupling). From the upper bounds  $R_{\mu^-e^-}(\text{Cu}) < 1.6 \times 10^{-8}$  [ref. <sup>12)</sup>] and  $R_{\mu^-e^-}(^{32}\text{S}) < 7 \times 10^{-11}$ , the following limits on these coupling constants can be derived:

$$|g_V^{(0)}| < 6.8 \times 10^{-7} \quad \text{and} \quad |g_V^{(1)}| < 2.8 \times 10^{-4}.$$

In a similar way we find

$$|g_S^{(0)}| < 7.1 \times 10^{-7} \quad \text{and} \quad |g_S^{(1)}| < 3.1 \times 10^{-4}$$

for the coupling constants of an effective hamiltonian involving scalar fermion currents [see also ref. <sup>57)</sup>].

**6.1.2. Neutral heavy leptons.** Muon-electron conversion may occur as a higher-order effect involving neutral heavy leptons (fig. 1). In a Weinberg-Salam model with massive neutrinos<sup>17)</sup>, the limit on  $R_{\mu^-e^-}(^{32}\text{S})$  can be used to constrain the range of possible masses and mixing angles of such neutral heavy leptons. In general, however, there are so many arbitrary parameters, that useful constraints can be obtained for special cases only; an example was given in our previous work<sup>34)</sup>. The known neutrinos are not affected by these constraints, since muon-electron conversion due to their possible finite masses is strongly suppressed by the smallness of these masses. Nonzero masses for the known neutrinos could however mean that other heavier neutrinos exist. Note that a minimal model<sup>58)</sup> without a  $\nu_\tau$  is excluded<sup>57)</sup> by the experimental upper limit on  $R_{\mu^-e^-}(^{32}\text{S})$  and the lifetime of the charged tau lepton.

**6.1.3. Neutral generation changing gauge bosons.** The upper limit on  $R_{\mu^-e^-}(^{32}\text{S})$  can be used to set an upper bound of the order of  $10^{-4} G_F$  on the effective strength of a “horizontal” interaction<sup>21)</sup> relating the different generations, and mediated by neutral generation changing gauge bosons. Technicolor schemes suggest<sup>22)</sup> that the effective strength of horizontal interactions might be close to this bound, and that muon-electron conversion might be found not far below the present experimental upper limit.

## 6.2. MUON-POSITRON CONVERSION

A phenomenological analysis of muon-positron conversion, in which the necessary double charge exchange in the nucleus arises mainly from  $\Delta \leftrightarrow N$  transitions, was given by Shuster and Rho<sup>59</sup>). The result  $R_{\mu^-e^+}(^{32}\text{S}) < 9 \times 10^{-10}$  can be used to set an upper limit on the effective ( $\mu^-e^+$ ) coupling constant  $G_{\mu^-e^+}$ :

$$G_{\mu^-e^+} < 2.6 \times 10^{-3} G_F.$$

Specific models<sup>29,31</sup>) predict muon-positron conversion branching ratios several orders of magnitude below the above-given experimental upper limit.

We are indebted to the SIN staff responsible for the accelerator, the beam pulser and the cryogenics, and to our technical staff, whose excellent work made this experiment possible. We thank P. Minkowski, H. Kaspar and R.P. Redwine for substantial contributions. We acknowledge also the great assistance by M. Hess and the careful picture evaluations by Mrs. M. Czapek and Mrs. V. Dvorak.

This work was financially supported by the Swiss National Science Foundation, SIN and the Canton of Berne.

## References

- 1) G. Feinberg, Phys. Rev. **110** (1958) 1482;  
F.J. Ernst, Phys. Rev. Lett. **5** (1960) 478
- 2) G. Feinberg and S. Weinberg, Phys. Rev. Lett. **3** (1959) 111, 244(E)
- 3) G. Danby *et al.*, Phys. Rev. Lett. **9** (1962) 36
- 4) G. Feinberg and S. Weinberg, Phys. Rev. Lett. **6** (1961) 381
- 5) E. Derman, Phys. Rev. **D19** (1979) 317
- 6) S.E. Willis *et al.*, Phys. Rev. Lett. **44** (1980) 522
- 7) E.J. Konopinski and H.M. Mahmoud, Phys. Rev. **92** (1953) 1045
- 8) P. Minkowski, Nucl. Phys. **B138** (1977) 527
- 9) J.D. Bowman *et al.*, Phys. Rev. Lett. **42** (1979) 556;  
A. van der Schaaf *et al.*, Nucl. Phys. **A340** (1980) 249
- 10) S. M. Korenchenko *et al.*, JETP (Sov. Phys.) **43** (1976) 1
- 11) A.R. Clark *et al.*, Phys. Rev. Lett. **26** (1970) 1667
- 12) D.A. Bryman, M. Blecher, K. Gotow and R.J. Powers, Phys. Rev. Lett. **28** (1972) 1469
- 13) J. Bailey *et al.*, Nucl. Phys. **B150** (1979) 1
- 14) E. di Capua *et al.*, Phys. Rev. **133** (1964) B1333;  
D. Bryman and C. Picciotti, Phys. Rev. **D11** (1975) 1337
- 15) For reviews see for example  
B. Humpert, Helv. Phys. Acta **50** (1977) 676;  
J. Schacher, Comments Nucl. Part. Phys. **8** (1978) 97;  
F. Scheck, Phys. Reports **44C** (1978) 187;  
B. Hahn and T. Marti, in Exotic atoms '79, eds. K. Crowe, G. Fiorentini and G. Torelli (Plenum, New York, 1980) p. 23
- 16) A. Salam, Elementary particle physics: relativistic groups and analyticity (Nobel Symp. no. 8), ed. N. Svartholm (Almqvist and Wiksell, Stockholm, 1968) p. 367;  
S. Weinberg, Phys. Rev. Lett. **19** (1967) 1264

- 17) G. Altarelli *et al.*, Nucl. Phys. **B125** (1977) 285;  
 B. W. Lee, S. Pakvasa, R.E. Shrock and H. Sugawara, Phys. Rev. Lett. **38** (1977) 937, 1230(E);  
 T.P. Cheng and L.-F. Li, Phys. Rev. Lett. **45** (1980) 1908
- 18) J.D. Bjorken and S. Weinberg, Phys. Rev. Lett. **38** (1977) 622
- 19) R.N. Mohapatra and G. Senjanovic, Phys. Rev. Lett. **44** (1980) 912
- 20) F. Wilczek and A. Zee, Phys. Lett. **88B** (1979) 311;  
 H. Georgi and D.V. Nanopoulos, Nucl. Phys. **B155** (1979) 52;  
 E. Witten, Phys. Lett. **91B** (1980) 81;  
 R. Barbieri, J. Ellis and M.K. Gaillard, Phys. Lett. **90B** (1980) 249
- 21) R. N. Cahn and H. Harari, Nucl. Phys. **B176** (1980) 135;  
 G.L. Kane and R. Thun, Phys. Lett. **94B** (1980) 513;  
 T. Maehara and T. Yanagida, Progr. Theor. Phys. **61** (1979) 2686;  
 O. Shanker, Phys. Rev. **D23** (1981) 1555
- 22) S. Dimopoulos and J. Ellis, Nucl. Phys. **B182** (1981) 505
- 23) E. Eichten and K. Lane, Phys. Lett. **90B** (1980) 125
- 24) W. J. Marciano and A.I. Sanda, Phys. Rev. Lett. **38** (1977) 1512
- 25) A. Lagarrigue and C. Peyrou, Compt. Rend. **234** (1952) 1873
- 26) J. Steinberger and H. B. Woolfe, Phys. Rev. **100** (1955) 1490;  
 R.D. Sard, K.M. Crowe and H. Kruger, Phys. Rev. **121** (1961) 619;  
 M. Conversi, L. di Lella, A. Egidi, C. Rubbia and M. Toller, Phys. Rev. **122** (1961) 687
- 27) G. Conforto *et al.*, Nuovo Cim. **26** (1962) 261;  
 J. Bartley, H. Davies, H. Muirhead and T. Woodhead, Phys. Lett. **13** (1964) 258
- 28) R.E. Marshak, Riazuddin and C.P. Ryan, Theory of weak interactions in particle physics (Wiley, New York, 1969), p. 66
- 29) A.N. Kamal and J.N. Ng, Phys. Rev. **D20** (1979) 2269;  
 J.D. Vergados and M. Ericson, Preprint CERN-TH 2982 (1980)
- 30) H. Primakoff and S.P. Rosen, Phys. Rev. **184** (1969) 1925
- 31) A. Zee, Phys. Lett. **93B** (1980) 389;  
 J.D. Vergados, Phys. Rev. **D23** (1981) 703
- 32) B. Pontecorvo, Sov. Phys. (JETP) **26** (1968) 984
- 33) A. Badertscher *et al.*, Phys. Rev. Lett. **39** (1977) 1385;  
 A. Badertscher *et al.*, Phys. Lett. **79B** (1978) 371
- 34) A. Badertscher *et al.*, Nuovo Cim. Lett. **28** (1980) 401
- 35) R. H. Helm, Phys. Rev. **104** (1956) 1466
- 36) Yu.I. Bely *et al.*, Nucl. Phys. **A204** (1973) 357;  
 M. Lifshitz and P. Singer, Phys. Rev. **C22** (1980) 2135
- 37) SIN Annual report 1977, p. A21;  
 P. Lanz, M. Märki and U. Schryber, SIN Newsletter **8** (1977) 7;  
 G. Czapek *et al.*, Nucl. Instr. **105** (1972) 609
- 38) G. Czapek *et al.*, Nucl. Instr. **157** (1978) 339
- 39) E. Gygi and F. Schneider, CERN 64-46 (1964)
- 40) CERN General Studies Group, CERN-ISR-GS/68-8 (1968)
- 41) V. Eckhardt and H.J. Gebauer, DESY Report 72/2 (1972)
- 42) H. Scheidiger *et al.*, Nucl. Phys. **A368** (1981) 438
- 43) M. Eckhouse, R.T. Siegel and R.E. Welsh, Nucl. Phys. **81** (1966) 575
- 44) A. Suzuki, Phys. Rev. Lett. **19** (1967) 1005
- 45) R.A. Eramzhyan, L. Majlinc, J. Rizek and R.A. Sakaev, Czech. J. Phys. **B28** (1978) 1081
- 46) H. Primakoff, Rev. Mod. Phys. **31** (1959) 802
- 47) F. Herzog and K. Alder, Helv. Phys. Acta **53** (1980) 53
- 48) R.D. Hart *et al.*, Phys. Rev. Lett. **39** (1977) 399
- 49) W. Heitler, The quantum theory of radiation (Oxford University Press, Oxford, 3rd ed., 1954) p 377
- 50) P. Hänggi, Master's thesis, University of Basel (1973), unpublished
- 51) N.M. Kroll and W. Wada, Phys. Rev. **98** (1955) 1355
- 52) See ref. <sup>49</sup>, p. 258f

- 53) L.M. Rosenstein and I.S. Hammerman, Phys. Rev. **C8** (1973) 603
- 54) R. Abela *et al.*, Phys. Lett. **95B** (1980) 318
- 55) L. Winsberg, Phys. Rev. **95** (1954) 205
- 56) O. Shanker, Phys. Rev. **D20** (1979) 1608
- 57) T. Marti, Doctoral thesis, University of Berne (1981), unpublished
- 58) G. Altarelli *et al.*, Phys. Lett. **67B** (1977) 463
- 59) M.D. Shuster and M. Rho, Phys. Lett. **42B** (1972) 45;  
M. Rho, 1972 SIN Spring School, p. 143ff